The Astrophysical Journal, 860:60 (16pp), 2018 June 10 https://doi.org/10.3847/1538-4357/aac20d

On the Transition of the Galaxy Quenching Mode at $0.5 < z < 1$ in CANDELS

F. S. Liu[1,2], Meng Jia[1], Hassen M. Yesuf[2], S. M. Faber[2], David C. Koo[2], Yicheng Guo[3], Eric F. Bell[4], Dongfei Jiang[1], Weichen Wang[5], Anton M. Koekemoer[6], Xianzhong Zheng[7], Jerome J. Fang[8], Guillermo Barro[9], Pablo G. Pérez-González[10], Avishai Dekel[11], Dale Kocevski[12], Nimish P. Hathi[6], Darren Croton[13], M. Huertas-Company[14], Xianmin Meng[15], Wei Tong[1], and Lu Liu[1]

[1] College of Physical Science and Technology, Shenyang Normal University, Shenyang 110034, People's Republic of China; fengshan.liu@yahoo.com
[2] University of California Observatories and the Department of Astronomy and Astrophysics, University of California, Santa Cruz, CA 95064, USA
[3] Department of Physics and Astronomy, University of Missouri, Columbia, MO 65211, USA
[4] Department of Astronomy, University of Michigan, Ann Arbor, MI, USA
[5] Department of Physics and Astronomy, Johns Hopkins University, 3400 N. Charles Street, Baltimore, MD 21218, USA
[6] Space Telescope Science Institute, 3700 San Martin Drive, Baltimore, MD 21218, USA
[7] Purple Mountain Observatory, Chinese Academy of Sciences, 2 West-Beijing Road, Nanjing 210008, People's Republic of China
[8] Astronomy Department, Orange Coast College, Costa Mesa, CA 92626, USA
[9] University of the Pacific, Department of Physics, 3601 Pacific Avenue Stockton, CA 95211, USA
[10] Departamento de Astrofísica, Facultad de CC. Físicas, Universidad Complutense de Madrid, E-28040 Madrid, Spain
[11] Center for Astrophysics and Planetary Science, Racah Institute of Physics, The Hebrew University, Jerusalem, Israel
[12] Department of Physics and Astronomy, Colby College, Mayflower Hill Drive, Waterville, ME 0490, USA
[13] Centre for Astrophysics and Supercomputing, Swinburne University of Technology, P.O. Box 218, Hawthorn, Victoria 3122, Australia
[14] Sorbonne Universit, Observatoire de Paris, Universit PSL, Universit Paris Diderot, CNRS, LERMA, Paris, France
[15] National Astronomical Observatories, Chinese Academy of Sciences, A20 Datun Road, Beijing 100012, People's Republic of China
Received 2018 February 3; revised 2018 April 29; accepted 2018 April 30; published 2018 June 12

Abstract

We investigate the galaxy quenching process at intermediate redshift using a sample of ∼4400 galaxies with $M_* > 10^9\ M_\odot$ between redshift 0.5 and 1.0 in all five CANDELS fields. We divide this sample, using the integrated specific star formation rate (sSFR), into four subgroups: star-forming galaxies (SFGs) above and below the ridge of the star-forming main sequence (SFMS), transition galaxies and quiescent galaxies. We study their *UVI* ($U-V$ versus $V-I$) color gradients to infer their sSFR gradients out to twice effective radii. We show that on average both star-forming and transition galaxies at all masses are not fully quenched at any radii, whereas quiescent galaxies are fully quenched at all radii. We find that at low masses ($M_* = 10^9$–$10^{10}\ M_\odot$) SFGs both above and below the SFMS ridge generally have flat sSFR profiles, whereas the transition galaxies at the same masses generally have sSFRs that are more suppressed in their outskirts. In contrast, at high masses ($M_* > 10^{10.5}\ M_\odot$), SFGs above and below the SFMS ridge and transition galaxies generally have varying degrees of more centrally suppressed sSFRs relative to their outskirts. These findings indicate that at $z \sim 0.5$–1.0 the main galaxy quenching mode depends on its already formed stellar mass, exhibiting a transition from "the outside-in" at $M_* \leqslant 10^{10}\ M_\odot$ to "the inside-out" at $M_* > 10^{10.5}\ M_\odot$. In other words, our findings support that internal processes dominate the quenching of massive galaxies, whereas external processes dominate the quenching of low-mass galaxies.

Key words: galaxies: high-redshift – galaxies: photometry – galaxies: star formation

1. Introduction

Studying the spatial distribution of the specific star formation rate (sSFR = SFR/M_*) is helpful to understand how stellar mass (M_*) is built up in galaxies as they evolve along the star formation main sequence (SFMS; Brinchmann et al. 2004; Elbaz et al. 2007; Noeske et al. 2007; Whitaker et al. 2014), and how and where the star formation shuts down as galaxies move off the SFMS to become fully quiescent. Broadly speaking, there are two types of processes responsible for cessation of star formation in galaxies: the internal and the external processes. The internal processes quench star formation due to the intrinsic properties of galaxies, such as central compaction (Fang et al. 2013; Liu et al. 2016; Barro et al. 2017; Whitaker et al. 2017), AGN feedback (Croton et al. 2006), and supernova feedback (Geach et al. 2014), which scale with the stellar mass of galaxies ("mass-quenching"; e.g., Peng et al. 2010; Kawinwanichakij et al. 2017). The internal processes first deplete the gas in the centers of galaxies or blow it out of the centers, causing "the inside-out" quenching. The external processes, like the environmental effects (e.g., Geha et al. 2012; Peng et al. 2012; Guo et al. 2017; Papovich et al. 2018), strip the gas content of galaxies first from their outskirts, causing "the outside-in" quenching. The two types of processes are expected to change the radial sSFR profile of a galaxy in a different way during its quenching process.

Encouraging progress has recently been made in understanding the radial gradients of sSFRs, traced by EW(Hα) and rest-frame UV–optical colors, in distant star-forming galaxies (SFGs; e.g., Nelson et al. 2012, 2016a, 2016b; Wuyts et al. 2012; Liu et al. 2016, 2017; Tacchella et al. 2018; Wang et al. 2017). These studies typically find either flat sSFR gradients (in galaxies with $M_* \lesssim 10^{10}\ M_\odot$ at $z \sim 1$ and galaxies with $M_* < 10^{11}\ M_\odot$ at $z \sim 2$) or somewhat centrally suppressed sSFRs (in galaxies with $M_* \gtrsim 10^{10.5}\ M_\odot$ at $z \sim 1$ and galaxies with $M_* > 10^{11}\ M_\odot$ at $z \sim 2$). A correction for dust gradient was shown to be one of the main sources of uncertainty that makes studying the sSFR gradients in distant SFGs challenging (Wuyts et al. 2013; Liu et al. 2016, 2017; Wang et al. 2017; Tacchella et al. 2018; Nelson et al. 2018).

Rest-frame *UVJ* ($U-V$ versus $V-J$) diagram has been widely used to separate quenched from dusty/SFGs (e.g., Wuyts et al. 2007; Williams et al. 2009; Brammer et al. 2011;

Patel et al. 2011). More recently, it has also been successfully utilized to determine sSFR and A_V values, which are broadly consistent with the values derived from fitting reddened stellar population models to broadband spectral energy distributions (SEDs) of galaxies covering UV to mid-infrared (Fang et al. 2018). Furthermore, Wang et al. (2017) demonstrated that the rest-frame *UVI* ($U-V$ versus $V-I$) diagram is as useful as the *UVJ* diagram for distinguishing sSFR from dust extinction.

In cosmological simulations, Tacchella et al. (2016a, 2016b) predict that, at high redshifts ($z=7-1$), the galaxy evolution across the SFMS is associated with events of wet compaction into compact star-forming systems, which trigger central gas depletion and the formation of an extended gas ring around it. The Tacchella et al. simulations reveal that the high-sSFR galaxies at the upper envelope of the SFMS and the lower-sSFR galaxies at the lower envelope of the SFMS have different properties, which is closely related to the quenching process of galaxies.

With the aim to understand the star formation quenching process in distant galaxies, in this work we select a sample of 4377 galaxies with $M_*>10^9\,M_\odot$ between redshifts 0.5 and 1.0 from all five CANDELS fields. With this sample, we investigate the *UVI* color gradients and inferred sSFR gradients in various galaxy populations (i.e., SFGs, transition galaxies, and quiescent galaxies). We specifically follow Tacchella et al. (2016a, 2016b) to divide our SFGs at intermediate redshifts into groups above and below the ridge of the SFMS, since this further classification is likely helpful to shed light on whether the shape of sSFR profiles start to vary during the evolution across the SFMS. We show that these different populations of galaxies have varying degrees of color and sSFR gradients. We find that the main quenching mode of a galaxy at $z\sim0.5-1$ depends on its already formed stellar mass, and it is outside-in for galaxies with $M_*\leqslant10^{10}\,M_\odot$, and inside-out for galaxies with $M_*>10^{10.5}\,M_\odot$. Throughout the paper, we adopt a cosmology with a matter density parameter $\Omega_m=0.3$, a cosmological constant $\Omega_\Lambda=0.7$ and a Hubble constant of $H_0=70$ km s^{-1} Mpc^{-1}. All magnitudes are in the AB system.

2. Data

CANDELS (Grogin et al. 2011; Koekemoer et al. 2011) is an *HST* Multi-Cycle Treasury Program to image portions of five commonly studied legacy fields (COSMOS, EGS, GOODS-N, GOODS-S, and UDS). The CANDELS group has made a multiwavelength photometry catalog for each field. Photometry in *HST*/WFC3 and ACS was measured by running `SExtractor` in the dual model on the point-spread function (PSF)-matched images, with the F160W image as the detection image. Photometry in the lower-resolution images (e.g., ground-based and IRAC) was measured using `TFIT` (Laidler et al. 2007). We refer readers to Guo et al. (2013), Galametz et al. (2013), Nayyeri et al. (2017), Stefanon et al. (2017), and G. Barro et al. (2018, in preparation) for details.

Redshifts used in this work are in the order of priority of secure spectroscopic (flagged as "very secure" or "reliable"), good grism (at least two users agree that it is good), and photometric redshifts if available. Spectroscopic redshifts were recently recompiled by N. P. Hathi (2018, private communication) for all five CANDELS fields, which include publicly available (e.g., Santini et al. 2015, and reference therein) and unpublic (e.g., UCR DEIMOS Survey) redshifts. Grism redshifts came from the 3D-*HST*/CANDELS Survey (e.g., Morris et al. 2015; Momcheva et al. 2016). Photometric redshifts were estimated using the multiwavelength photometry catalogs and adopting a hierarchical Bayesian approach (Dahlen et al. 2013). The typical scatter of photometric redshifts spans from 0.03 to 0.06 in $\Delta(z)/(1+z)$. Rest-frame integrated magnitudes from *FUV* to *K* were computed using `EAZY` (Brammer et al. 2008), which fits a set of galaxy SED templates to the multiwavelength photometry, with the redshifts as inputs.

Stellar masses were computed using `FAST` (Kriek et al. 2009) and based on a grid of Bruzual & Charlot (2003) models that assume a Chabrier (2003) IMF, declining τ-models, solar metallicity, and a Calzetti et al. (2000) dust law. The typical formal uncertainty in stellar mass is $\sim$0.1 dex. SFRs were computed from rest-frame UV luminosities at $\lambda\approx2800$ Å that are corrected for extinction by applying a foreground-screen Calzetti reddening law ($A_{2800}\approx1.79A_V$): $\mathrm{SFR_{UV,cor}}[M_\odot\,\mathrm{yr}^{-1}]=2.59\times10^{-10}L_{\mathrm{UV,cor}}[L_\odot]$ (Kennicutt & Evans 2012). Fang et al. (2018) showed that the sSFRs by this method are consistent with those derived from UV and far-IR luminosities in a broad range, with a typical scatter of $\sim$0.2 dex. We adopted the median A_V that was calculated by combining results from four methods (see labeled $2a_\tau$, $12a$, $13a_\tau$, and $14a$ in Santini et al. 2015) if available. These methods were chosen based on the same assumptions (Chabrier IMF and the Calzetti dust law). The typical formal uncertainty in A_V is $\sim$0.1 mag. Effective radius along the semimajor axis (R_{SMA}) and minor-to-major axis ratio (q) were measured from the F125W images using `GALFIT` (Peng et al. 2002) by van der Wel et al. (2012).

Spatially resolved data is taken from the *HST*-based multiband and multiaperture photometry catalogs of CANDELS still under construction by F. S. Liu et al. (2018, in preparation). These data sets include the radial profiles of isophotal ellipticity (ε) and disky/boxy parameter A_4 in both F125W and F160W, and the observed surface brightness profiles (SBPs) in all *HST*/ACS (F435W, F606W, F775W, F814W, and F850LP) bands and WFC3 (F105W, F125W, F140W, and F160W) bands if available. Preliminary imaging reduction prior to multiaperture photometry can be found in Jiang et al. (2018). The photometry was done by using the `IRAF` routine `ellipse` within STSDAS, which is based on a technique described by Jedrzejewski (1987). For galaxies used in this work, we fixed the galaxy geometric centers, ellipticities, and position angles obtained from the `GALFIT` measurements along the semimajor axes for all available bands. Rest-frame *U*, *V*, and *I* band SBPs were then computed using `EAZY` (Brammer et al. 2008) by fitting the best-fit SEDs in each photometry annulus (refer to Figure 2 in Liu et al. 2016).

3. Sample Selection

In order to maximize the sample size, we select galaxies from all five CANDELS fields by applying the following criteria to the above catalogs:

1. Observed F160W(H) magnitude brighter than 24.5 to ensure high signal-to-noise ratios (S/Ns).
2. `SExtractor` PhotFlag = 0 and CLASS_STAR < 0.9 to exclude spurious sources and stars.
3. Redshifts within $0.5<z<1$ and stellar masses $M_*>10^9\,M_\odot$ to maintain high-mass completeness and to

Table 1
Sample Selection Criteria and the Resulting Sample Sizes for Each Field

Criterion	GOODS-S	UDS	GOODS-N	EGS	COSMOS	Combined
Full Catalog	34930(100%)	35932(100%)	35445 (100%)	41457(100%)	38671(100%)	186435(100%)
Hmag < 24.5	8293(23.74%)	9671(26.91%)	9460(26.69%)	11292(27.24%)	11811(30.54%)	50527(27.10%)
PhotFlag $= 0$	8104(23.20%)	9151(25.47%)	9011(25.42%)	7521(18.14%)	7603(19.66%)	41084(22.04%)
CLASS_STAR < 0.9	7901(22.62%)	8952(24.91%)	8815(24.87%)	7252(17.49%)	7297(18.86%)	40217(21.57%)
$0.5 < z < 1.0$	2460(7.04%)	2331(6.49%)	2746(7.75%)	1950(4.70%)	2457(6.35%)	11944(6.41%)
$\log M/M_{\odot} > 9.0$	1291(3.70%)	1293(3.60%)	1632(4.60%)	952(2.30%)	1428(3.69%)	6596(3.54%)
GALFIT Flag(J) $= 0$ or 1	1232(3.53%)	1246(3.47%)	1572(4.44%)	933(2.25%)	1373(3.55%)	6356(3.41%)
$R_{\rm SMA} > 0.''18$	1092(3.13%)	1089(3.03%)	1369(3.86%)	814(1.96%)	1181(3.05%)	5545(2.97%)
Accurate Multiband SBPs	963(2.76%)	828(2.30%)	1210(3.41%)	681(1.64%)	695(1.80%)	4377(2.38%)

guarantee the accuracy of rest-frame U, V, and I band spatially revolved data. Note that the *HST* imaging in CANDELS ends at the observed H band, which roughly corresponds to the rest-frame I band for galaxies at $z = 1$.

4. GALFIT quality flag $= 0$ (good fit) or flag $= 1$ (suspicious fit) in F125W (van der Wel et al. 2012) to ensure well-constrained measurements of structural parameters (i.e., effective radius and minor-to-major axis ratio) and eliminate mergers and disturbed objects.
5. $R_{\rm SMA} > 0.''18$ (3 drizzled pixels) to minimize the PSF effects on color gradient measurement. This lack of sample completeness cannot be avoided for this study given the limited resolution of *HST* imaging (see Appendices B and C).
6. Accurate simultaneous measurements of the SBPs from center to $2R_{\rm SMA}$ in at least two ACS bands and two WFC3 bands to guarantee the accuracy of SED modeling in each photometry annulus. Almost all (∼98%) of galaxies after this cut have accurate multiaperture photometry in F606W, F814W, F125W, and F160W, which cover all three rest-frame U, V, and I bands at $0.5 < z < 1$.

Table 1 details our selection criteria and the resulting sample sizes after each cut for each field. A detailed discussion on sample completeness by these criteria is given in Appendix B. After cuts 1–5, we select 5545 galaxies in total from all five CANDELS fields. Furthermore, 4377 galaxies remain after the sixth cut, of which we utilized their spectroscopic redshifts for 1132 (∼25.86%) galaxies, grism redshifts for 2152 (∼49.17%) galaxies and photometric redshifts for 1093 (∼24.97%) galaxies. Figure 1 shows the distributions of galaxies on the *UVJ* and *UVI* planes for the total sample and a nearly face-on ($q > 0.5$) subsample after cuts 1–5, respectively. It can be seen that *UVI* reproduces all the main features of *UVJ*, including the quenched region and the distinctive stripe patterns of sSFR, which is in agreement with the results initially presented by Wang et al. (2017). In Appendix A, we show that these main features on *UVJ* and *UVI* diagrams are still strong for UV+IR rates, which strengths our analysis in this work. However, given that SFRs involving IR data are subject to their own set of systematic biases (see Appendix A), it is reasonable to adopt the UV-based rates.

In Figure 2, we show the sSFR–mass relation for our final sample of galaxies. Recent works (e.g., Whitaker et al. 2014; Lee et al. 2015) showed that the SFMS is not consistent with a single power law at $0.5 < z < 2.5$. Instead, it is better fitted by a broken power law, such that below a characteristic mass (M_c) of $M_c \sim 10^{10.2}\ M_{\odot}$, the SFMS has a redshift-independent slope of $\alpha \sim 1.0$. Above M_c, the SFMS has a shallow slope. At $0.5 < z < 1$, the characteristic mass is $\log(M_c/M_{\odot}) = 10.0 \pm 0.1$ (Whitaker et al. 2014; Tomczak et al. 2016). As such, the feature is obvious in our data. To derive the SFMS relation of our galaxies, an initial fit to all *UVJ*-defined SFGs is made; objects more than 2σ away from the fit are then excluded for the next fit. This fitting process is repeated until no new objects are excluded. The best broken power-law fits to the SFMS of our galaxies are shown as black lines in Figure 2, and are described by the following equations: $\log {\rm sSFR_{UV,cor}}/{\rm yr}^{-1} = 0.02 \pm 0.02[\log M_*/M_{\odot} - 10] - 8.91 \pm 0.12$ for $M_* \leqslant 10^{10} M_{\odot}$, and $\log {\rm sSFR_{UV,cor}}/{\rm yr}^{-1} = -0.41 \pm 0.03[\log M_*/M_{\odot} - 10] - 8.91 \pm 0.12$ for $M_* > 10^{10} M_{\odot}$.

To quantify the relative star formation activity in galaxies in a given mass bin, we compute the vertical offsets in $\log {\rm sSFR_{UV,cor}}$ from the best-fit SFMS. The offset for a given galaxy is denoted by $\Delta\log {\rm sSFR_{UV,cor}}$. Galaxies lying above (below) the best-fit SFMS are defined to have positive (negative) residuals. We then adopt $\Delta \log {\rm sSFR_{UV,cor}}$ to divide our galaxies into the following four subgroups:

a. $\Delta{\rm logsSFR_{UV,cor}} \geqslant 0$—SFGs above the SFMS ridge,
b. -0.45 dex $\leqslant \Delta \log {\rm sSFR_{UV,cor}} < 0$—SFGs below the SFMS ridge,
c. -1.2 dex $\leqslant \Delta \log {\rm sSFR_{UV,cor}} < -0.45$ dex—transition galaxies,
d. $\Delta \log {\rm sSFR_{UV,cor}} < -1.2$ dex—quiescent galaxies. The use of this relative quantity ($\Delta\log {\rm sSFR_{UV,cor}}$) for classification means that our results are insensitive to the exact zero points and slopes of the fits.

The SFMS has a dispersion of $\sigma \sim 0.3$ dex in the logarithmic scale. The two thresholds of $\Delta\log {\rm sSFR_{UV,cor}} = -0.45$ dex (blue lines) and $\Delta\log {\rm sSFR_{UV}}$,cor $= -1.2$ dex (red lines) correspond to 1.5σ and 4σ below the ridge of the SFMS, respectively. We have checked that a change of ± 0.1 dex for our thresholds does not affect our conclusions.

4. Results and Analysis

Following the work of Wang et al. (2017), in Figure 3, we show raw stacked *UVI* color trajectories in *UVI*-space for four subgroups of total sample galaxies in four stellar mass bins, $9.0 < \log M_*/M_{\odot} \leqslant 9.5$, $9.5 < \log M_*/M_{\odot} \leqslant 10.0$, $10.0 < \log M_*/M_{\odot} \leqslant 10.5$, and $\log M_*/M_{\odot} > 10.5$, respectively. Color profiles in the same mass bins are stacked by first normalizing the radial positions of each galaxy by its $R_{\rm SMA}$ and then computing the median colors at the selected normalized positions. In each panel, five radial locations are indicated by solid circles with increasing size, ranging from $0.2\ R_{\rm SMA}$ at the

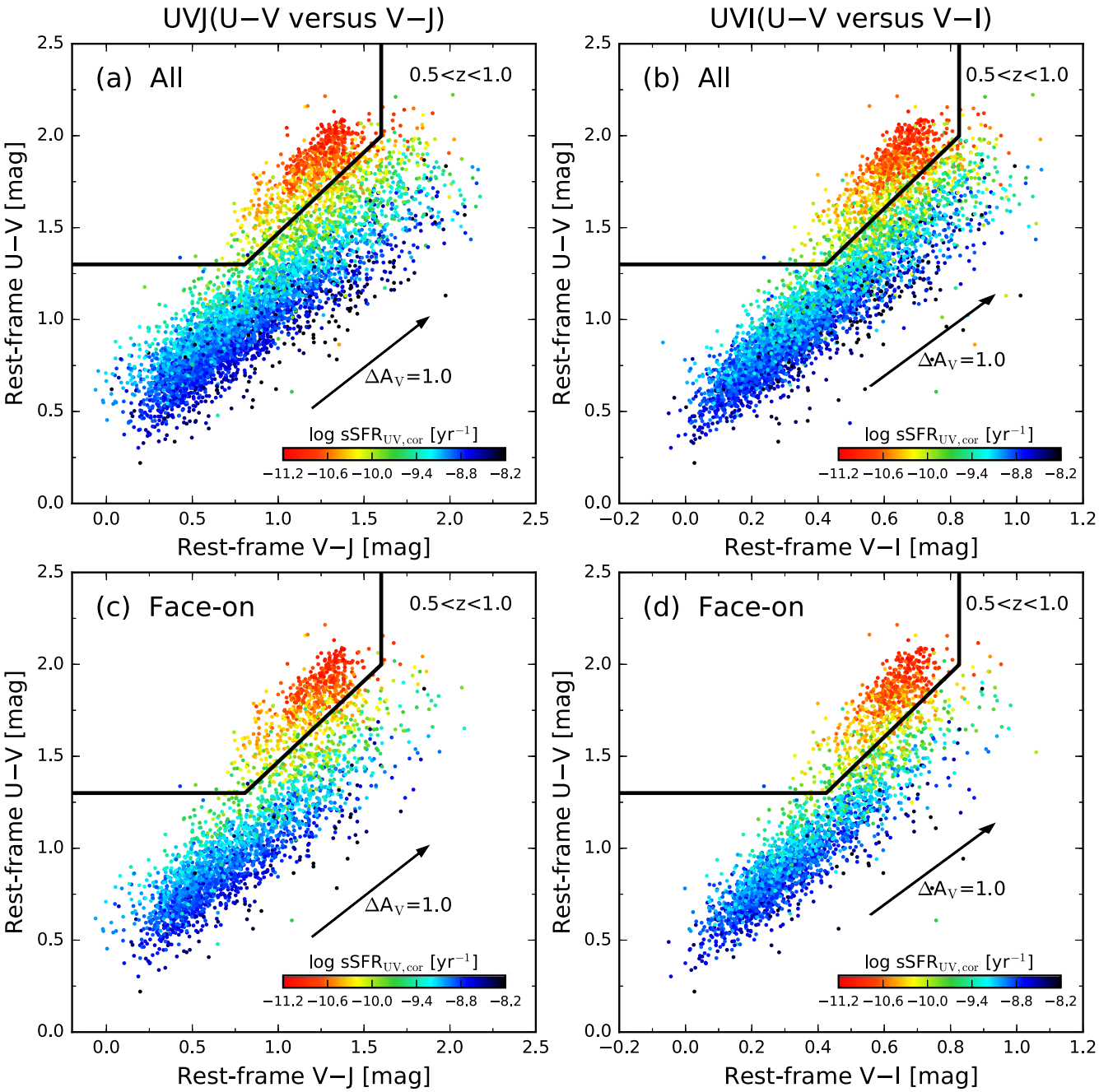

Figure 1. Rest-frame global *UVJ* diagrams (left) and *UVI* diagrams (right) for our total sample (top) and the face-on ($q > 0.5$) subsample (bottom) after applying the selection criteria 1–5, respectively. Data points are color-coded by log $\mathrm{sSFR}_{\mathrm{UV,cor}}$. Solid lines in *UVJ* diagrams indicate the boundary of Williams et al. (2009) to separate quiescent from star-forming galaxies. For *UVI*, the boundary lines are determined by visually confirming that objects on the *UVJ* boundaries also lie on the boundary lines in *UVI*. The arrows indicate the Calzetti reddening vector.

innermost to 2.0 R_{SMA} at the outermost. The arrows indicate the Calzetti reddening vector. The typical errors of the stacked colors are given for each panel, which are the average of the standard errors of median colors at all radii. An example is given in Appendix D to illustrate our estimate on the standard errors of median colors at a given radius. In addition, we correct the PSF effects by adopting the method of Szomoru et al. (2011). The corrected light profiles are first generated by adding the residuals from fitting the raw light profiles with the PSF-convolved single Sérsic model (Sérsic 1968) onto the Sérsic profiles. The resultant color trajectories are overplotted as magenta solid curves with increasing radii indicated by an arrow in Figure 3. As can be seen, the PSF correction stretches the length of color gradients on the *UVI* diagram by making galaxy colors slightly redder in the centers and bluer in the outskirts. However, the overall effect on color gradients is not large, which is consistent with our evaluation in Appendix C and that by Wang et al. (2017). To minimize the interplay between stellar population and dust reddening changes, in Figure 4, we additionally show the *UVI* color trajectories for a

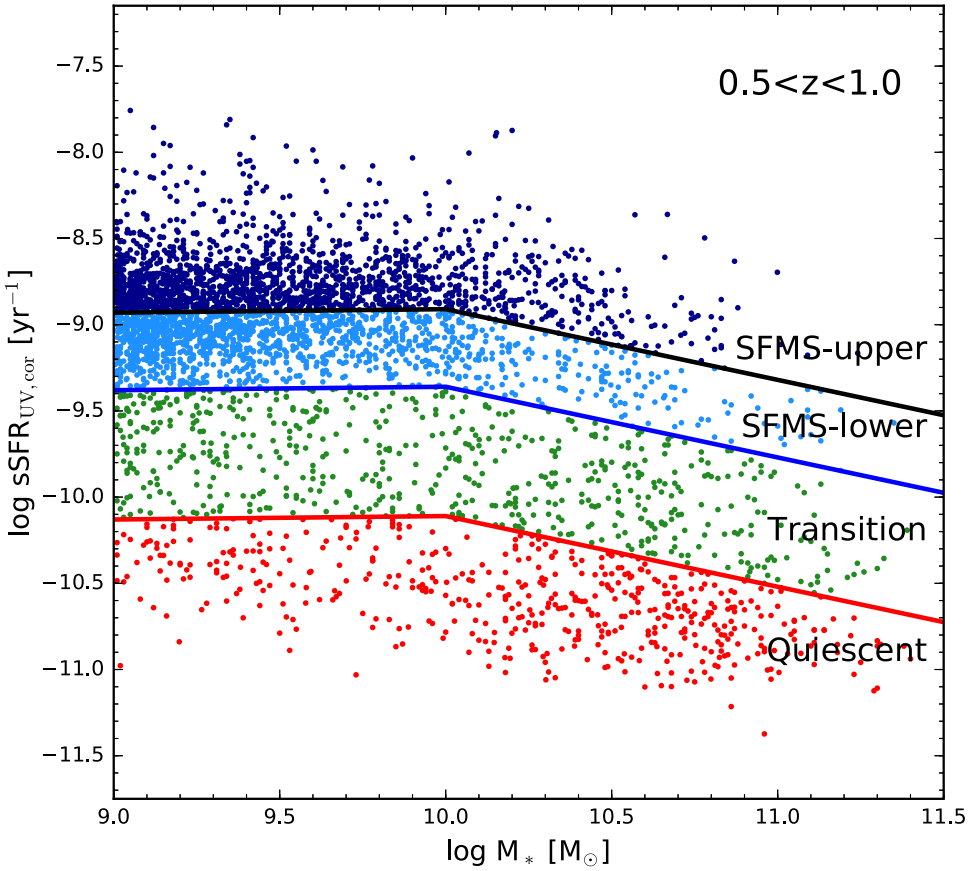

Figure 2. sSFR–mass relation for our final sample of galaxies. Black lines are the best broken power-law fits to the SFMS (namely Δ log sSFR$_{\rm UV,cor} = 0$). Blue lines indicate Δ log sSFR$_{\rm UV,cor} = -0.45$. Red lines indicate Δlog sSFR$_{\rm UV,cor} = -1.2$. Three boundary lines are combined to divide our galaxies into four subgroups: SFGs above and below the SFMS ridge (SFMS-upper and SFMS-lower), transition galaxies and quiescent galaxies. Four subgroups are shown with dots in different colors.

subsample of nearly face-on ($q > 0.5$) galaxies. These two figures for the two samples are similar. Main features in common are listed as follows:

1. For all mass ranges, all median color data points of SFGs both above and below the SFMS ridge lie well within the star-forming region. For high-mass transition galaxies with $M_* > 10^{10}\,M_\odot$, all of their median colors lie close to the boundary that separates quenched from non-quenched galaxies. On the other hand, all median colors except for the ones in the outer regions ($2.0R_{\rm SMA}$) of low-mass ($M_* = 10^9$–$10^{10}\,M_\odot$) transition galaxies lie still in the star-forming region of the *UVI* diagram. The median colors of quiescent galaxies at all radii lie well within the quenched region for all mass ranges.
2. The magnitudes of trajectories of SFGs are much larger than those of transition and quiescent galaxies. This is likely due to significant amounts of dust reddening in SFGs, because the magnitudes of their trajectories are elongated along the direction of reddening vector.
3. The trajectories of SFGs both above and below the SFMS are roughly parallel to the reddening vector, except that the centers in most massive bins obviously deviate toward the quenched region and the slight upturns appear in the outermost parts near $2.0R_{\rm SMA}$. These features have been captured for the entire population of SFGs and have been well studied by Wang et al. (2017).
4. The color trajectories of transition galaxies with $M_* > 10^{10}M_\odot$ and those with $M_* = 10^9$–$10^{10}\,M_\odot$ have different shapes, which indicates that the low-mass galaxies and high-mass galaxies have different sSFR gradients.

We now turn to the task of converting *UVI* color trajectories into the sSFR profiles following the method of Wang et al. (2017). To create the maps of sSFR on the *UVI* planes of Figures 1(b) and (d), we first divide each distribution into multiple 0.05×0.1 mag rectangles. In each rectangle, we compute the median CANDELS values of integrated sSFR and assign them to the center of the rectangle. Then, given any position on each *UVI* plane, the corresponding sSFR values can be obtained by linearly interpolating among the nearby rectangle centers. This method makes it possible to deduce sSFR values from *UVI* with an rms accuracy of $\sim$0.15 dex (see Section 3 in Wang et al. 2017). Adopting this calibration, the PSF-corrected *UVI* color trajectories are converted to radial sSFR profiles, as shown in Figure 5. It can be seen that, for lower-mass bins ($M_* = 10^9$–$10^{10}\,M_\odot$), SFGs both above and below the SFMS ridge generally have flat sSFR profiles, whereas the transition galaxies in the same mass ranges generally have negative sSFR gradients (sSFRs in the outskirts are more suppressed). In contrast, for the most massive bins ($M_* > 10^{10.5}\,M_\odot$), SFGs above and below the SFMS ridge and transition galaxies generally have varying degrees of positive sSFR gradients (more centrally suppressed sSFRs

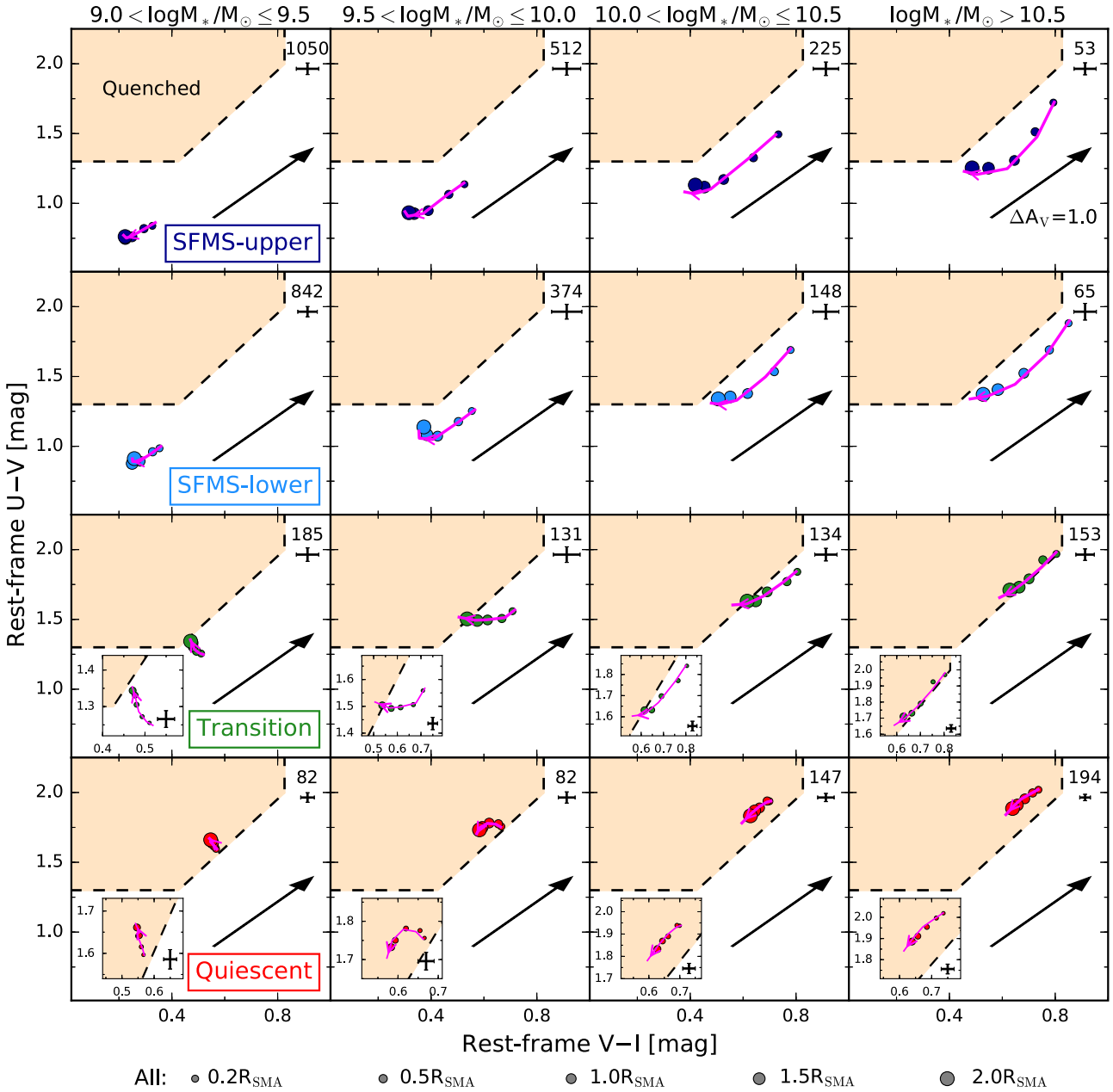

Figure 3. Rest-frame *UVI* color gradients for all SFGs above and below the SFMS ridge (SFMS-upper and SFMS-lower), transition galaxies and quiescent galaxies from top to bottom in four mass bins, respectively, as indicated in the top margin. For each panel, raw stacked data without correction for PSF smearing are shown by solid circles with increasing size. Magenta solid curves with an arrow indicate the radial trajectories after PSF correction, ranging from $0.2R_{\rm SMA}$ to $2R_{\rm SMA}$. Dashed lines indicate the boundary to separate quiescent from star-forming galaxies. The arrows indicate the Calzetti reddening vector. The average standard deviations of the stacked colors are shown in upper right. The galaxy number in each panel is shown in the top right corner as well. An inserted zoom-in plot is given specifically for quiescent and transition galaxies to display the details on small scales.

relative to their outskirts). As expected, nearly flat or relatively weak sSFR gradients are observed in quiescent galaxies at all masses. The outside-in quenching for lower-mass bins is indicated by the drop in sSFR of the transition galaxies, whereas the inside-out quenching for the most massive bins is best indicated by the rising sSFR of the lower SFMS galaxies. The results from inferred sSFRs are in good agreement with those from the directly observed data of *UVI* color gradients.

5. Discussion and Conclusion

We select a sample of 4377 large ($R_{\rm SMA} > 0\farcs18$) galaxies with $M_* > 10^9\,M_\odot$ between redshift 0.5 and 1.0 in all five CANDELS fields. These galaxies have well-measured, *HST* multiband multiaperture photometry data within $R < 2.0R_{\rm SMA}$ in CANDELS. We investigate the stacked *UVI* color gradients and inferred sSFR gradients in various galaxy populations (quiescent galaxies, transition galaxies, and SFGs divided into groups above and below the ridge of the SFMS) in different mass bins.

We show that, for all mass ranges, SFGs, on average, are not fully quenched at any radii, above the resolution limit of $0\farcs18$ ($\sim$1.3 kpc), whereas quiescent galaxies are fully quenched at all radii above this limit for all mass ranges. At all radii, the median *UVI* colors of high-mass transition galaxies with $M_* > 10^{10}\,M_\odot$ lie close to the boundary that separates

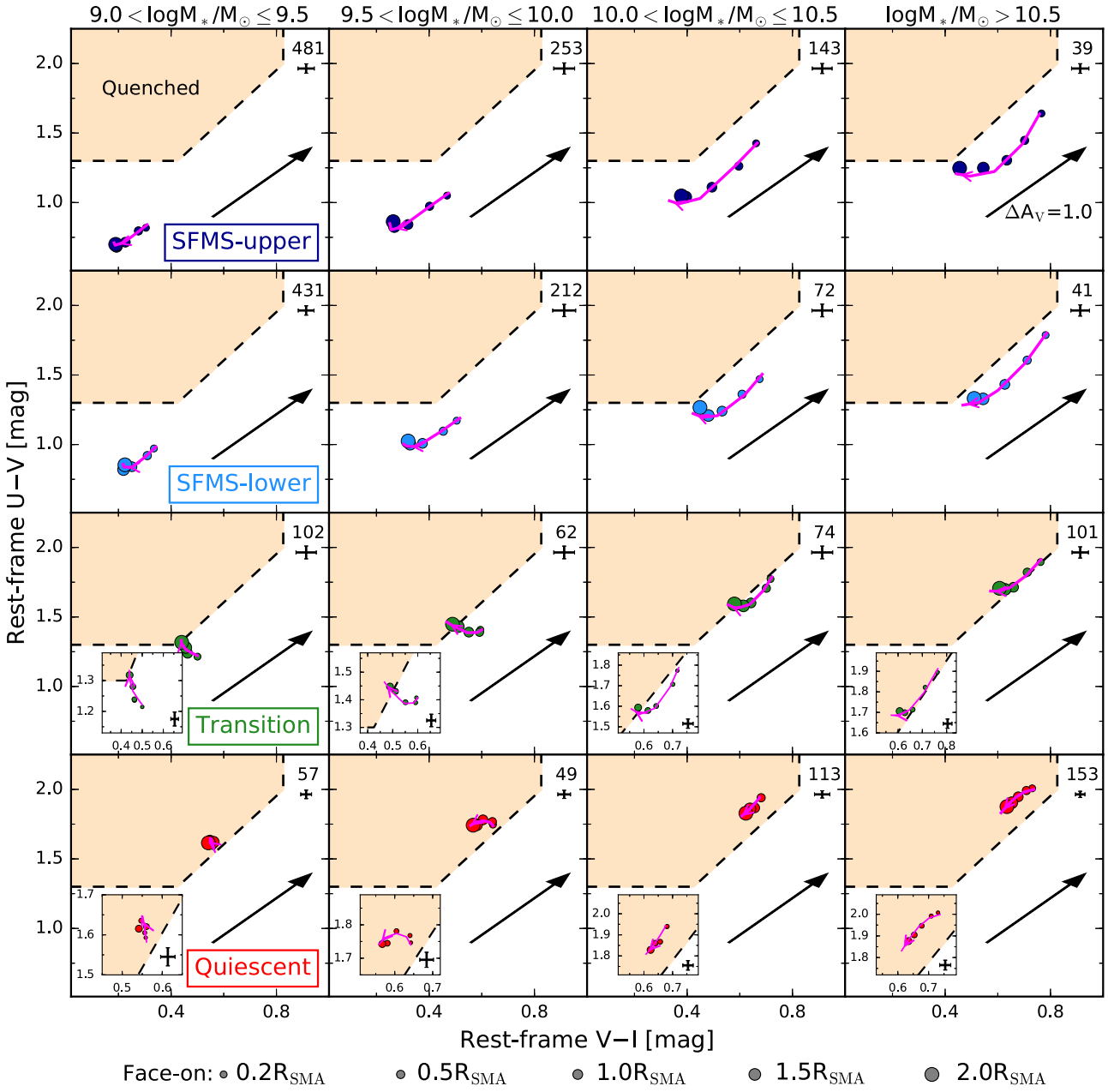

Figure 4. Same as Figure 3 but here only nearly face-on ($q > 0.5$) galaxies are shown.

quenched from nonquenched galaxies in the UVI diagram. In contrast, all median colors except for the ones in the outer regions ($2.0R_{\rm SMA}$) of low-mass ($M_* = 10^9 - 10^{10}\ M_\odot$) transition galaxies still lie in the star-forming region of the *UVI* diagram.

At low masses ($M_* = 10^9$–$10^{10}\ M_\odot$), SFGs both above and below the SFMS ridge generally have flat sSFR profiles, whereas the transition galaxies at the same masses have sSFRs that are more suppressed in the outskirts. In contrast, at high masses ($M_* > 10^{10.5}\ M_\odot$), SFGs above and below the SFMS ridge and transition galaxies have varying degrees of more centrally suppressed sSFRs relative to their outskirts. These findings indicate that at $z \sim 0.5$–1.0 the main galaxy quenching mode depends on its already formed stellar mass, exhibiting a transition from "the outside-in" at $M_* \leqslant 10^{10}\ M_\odot$ to "the inside-out" at $M_* > 10^{10.5}\ M_\odot$. The sSFR profiles in massive galaxies start to vary when they are on the SFMS, whereas the sSFR profiles in the lower-mass galaxies start to vary when they move off the SFMS. A similar trend is also observed in local galaxies (Pérez et al. 2013; Pan et al. 2015; Belfiore et al. 2017). This pattern is broadly consistent with the prediction of Tacchella et al. (2016a, 2016b) in cosmological simulations that a transition from outside-in to inside-out quenching occurs near a critical mass, $M_* \sim 10^{10}\ M_\odot$. Our results support the fact that the internal processes (i.e., central compaction, AGN feedback, and supernova feedback) dominate the quenching of massive galaxies, whereas the external processes (i.e., environmental effects) dominate the quenching of low-mass galaxies.

We have checked that our main results are unchanged under the stacking by physical radius rather than scaled radius. We stress that the inferred sSFR gradients are in good agreement

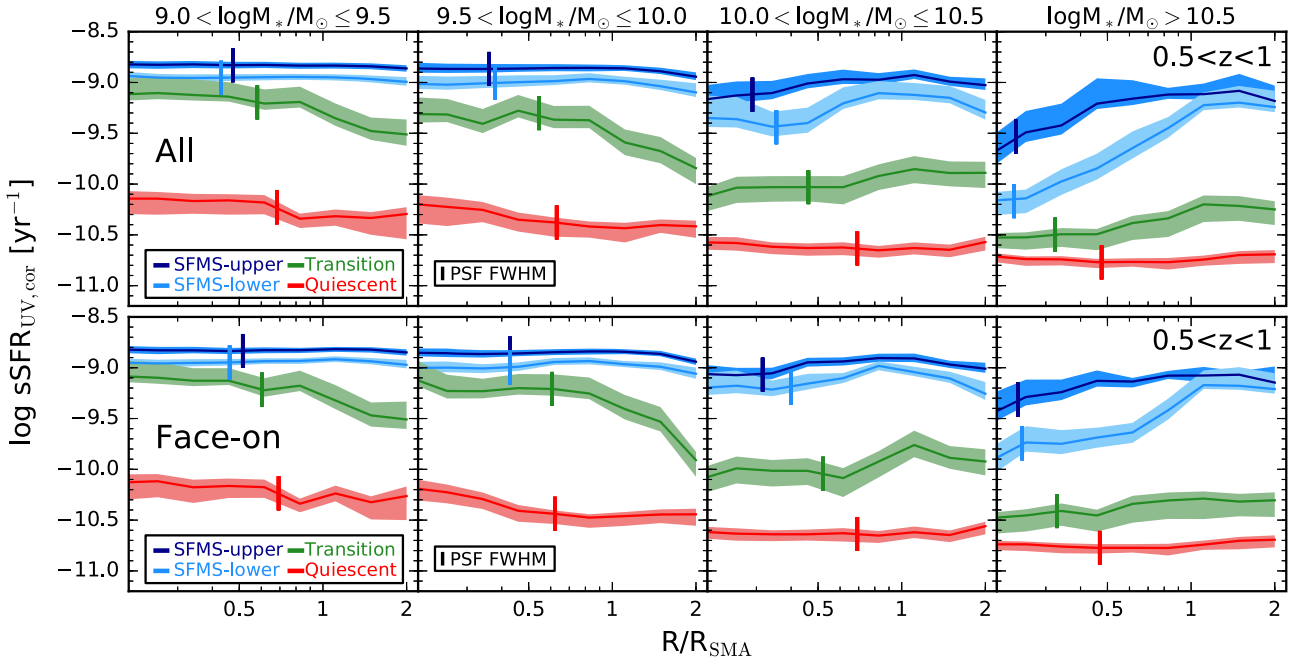

Figure 5. Stacked sSFR profiles of our total sample (top) and a nearly face-on subsample (bottom), which are inferred from the PSF-corrected *UVI* color trajectories as in Figures 3 and 4, respectively. Radial distance is scaled by the median angular size $R_{\rm SMA}$ of each subgroup in each mass bin. Curves in different colors denote different subgroups. Mass ranges are annotated at the top. Colored shadows denote the standard uncertainty of the stacked profiles, which include the uncertainty of the PSF correction and the standard deviation of the stacked color trajectories. Short vertical lines indicate the median PSF FWHM ($0\farcs18$) of each subgroup. The outside-in quenching for lower-mass bins is indicated by the drop in sSFR of the transition galaxies in green, whereas the inside-out quenching for the most massive bins is best indicated by the rising sSFR of the lower SFMS galaxies in blue.

with our raw data of *UVI* color gradients. The former, however, depends on the conventional SED modeling assumptions (i.e., τ-models, solar metallicity, and a foreground-screen Calzetti reddening law). We refer the reader to Wang et al. (2017) for discussions about the effects of these assumptions on sSFR gradients in SFGs (see Section 8.2 and the Appendix in their paper). The Wang et al.'s critique shows that, as long as stellar populations are reasonably uniform throughout a galaxy, these assumptions do not significantly affect the gradients in SFGs. It is still unclear what biases these assumptions can bring to the inferred sSFR gradients in transition and quiescent galaxies. The star formation histories of these populations are different from those of SFGs. Nevertheless, the resulting sSFR gradients in these populations based on the standard assumptions are consistent with the observed *UVI* color gradients, which are independent of any assumptions.

We caution that there are important ambiguities for highly quenched populations, due to the degeneracies among the effects of dust, stellar age, and metallicity on color gradients. Therefore, our conclusions for these objects are tentative. When we convert their color trajectories to sSFR gradients, we find no significant trend for the most massive bins. If these objects contain little or no dust (see Figure 11 in Fang et al. 2018) and their age (sSFR) gradients are flat, as shown in Figure 5, metallicity effects would play an important role. This is quite similar to the origin of optical color gradients in nearby early-type galaxies (e.g., Wu et al. 2005). In contrast, for lower-mass bins, we indeed see a trend that the centers are slightly younger than the outer parts. This trend is indicated by a clear transverse motion of the gradients across loci of constant sSFRs. Overall, the resulting quiescent trend agrees with a similar trend in transition galaxies at the same masses, suggesting that the two classes of galaxies are evolutionarily linked, as we would expect, since the mass difference between transition and quiescent galaxies should be small. We also caution that perhaps gradients in lower-mass quiescent galaxies cannot be resolved simply because they are too small. Future works should investigate the consequences of more realistic stellar population models, metallicity, and dust extinction law.

We acknowledge the anonymous referee for constructive comments and suggestions that significantly improved this paper. We thank Steven Willner for helpful comments on the manuscript, and Shude Mao for useful discussion. We acknowledge support from the NSF grants of China (11573017,11733006) and the CANDELS program *HST*-GO-12060 by NASA through a grant from the STScI. Space Telescope Science Institute, which is operated by the Association of Universities for Research in Astronomy, Incorporated, under NASA contract NAS5-26555. This work is partly based on observations taken by the 3D-*HST* Treasury Program (GO 12177 and 12328) with the NASA/ESA *HST*, which is operated by the Association of Universities for Research in Astronomy, Inc., under NASA contract NAS5-26555. S.M.F., D.C.K., Y.G., and H.M.Y. acknowledge partial support from US NSF grant AST-16-15730. P.G.P.-G. acknowledges support from Spanish Government MINECO AYA2015-70815-ERC and AYA2015-63650-P Grants.

Appendix A
$s\mathrm{SFR}_{\rm UV+IR}$ Patterns on *UVJ* and *UVI* Planes

We follow the Rujopakarn et al. (2013) method to derive $L_{\rm IR}$ of our sample galaxies. Only F160W objects that are identified as the nearest neighbor to an MIPS source are retained. As a result, of 5545 galaxies satisfying our selection criteria 1–5, 3790 ($\sim$70%) have S/N $>$ 1 MIPS 24 μm detections, 957 are

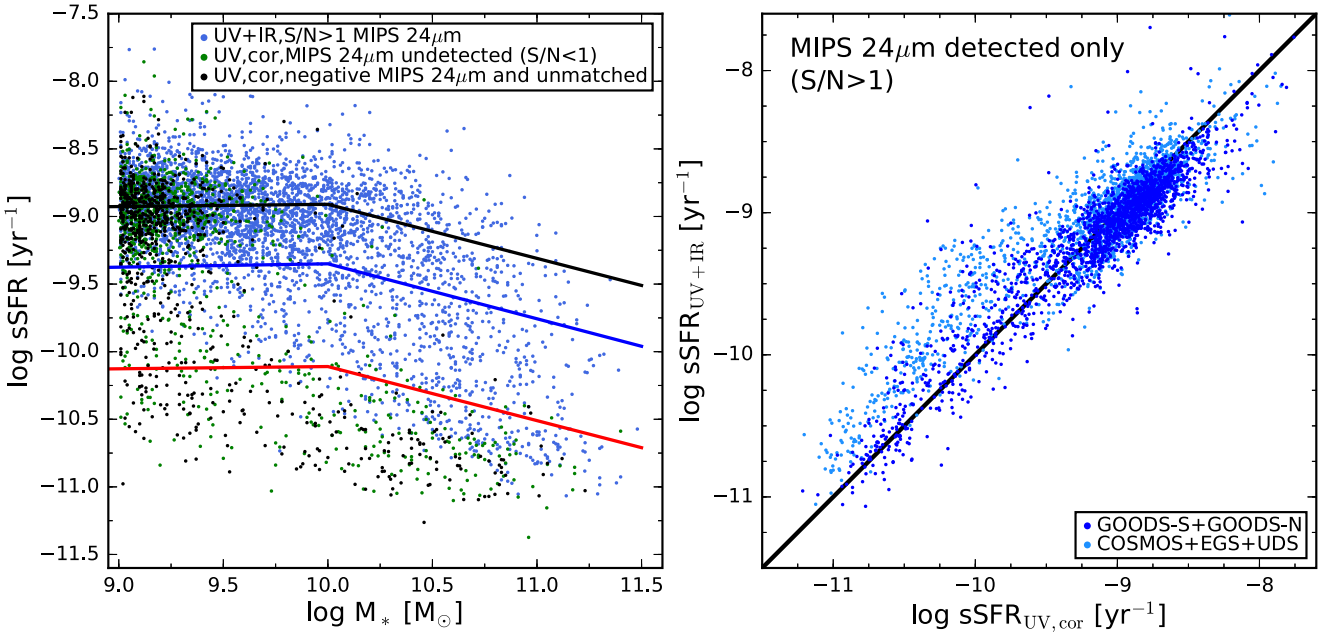

Figure 6. sSFR–mass relation for all galaxies after the cuts 1–5 (left) and $sSFR_{UV+IR}$ versus $sSFR_{UV,cor}$ for MIPS-detected subsample only (right). In the left panel, blue dots denote galaxies with S/N > 1 MIPS 24 μm detections. Green dots denote galaxies undetected in MIPS 24 μm photometry (S/N < 1). Black dots denote galaxies that either have negative MIPS 24μm fluxes or are unmatched sources. Solid lines have the same meanings as those in Figure 2. In the right panel, galaxies with the deepest IR data in GOODS-S and GOODS-N and galaxies in the other three fields (COSMOS, EGS, and UDS) are shown in different colors.

undetected in MIPS 24 μm photometry (S/N < 1), 782 have negative MIPS 24 μm fluxes, and 16 are unmatched. We then use the formula presented in Wuyts et al. (2011) to calculate the UV+IR SFRs for MIPS-detected subsample:

$$\mathrm{SFR_{UV+IR}}[M_\odot \mathrm{yr}^{-1}] = 1.09 \times 10^{-10}(L_{\mathrm{IR}} + 3.33L_{\mathrm{UV}})[L_\odot], \quad (1)$$

where L_{IR} is the integrated 8–1000 μm luminosity inferred from MIPS 24 μm, and $\mathrm{L_{UV}} \equiv \nu L_\nu(2800\,\text{Å})$ is the rest-frame near-UV luminosity, measured at 2800 Å. In Figure 6, we replot the sSFR–mass relation of all galaxies (left) and make a direct comparison between $sSFR_{UV,cor}$ and $sSFR_{UV+IR}$ for 24 μm detected objects only (right). As can be seen, in our redshift range, the UV+IR rates are biased at lower masses and for lower-sSFR objects. The UV-based method tends to slightly overestimate the SFRs for high-sSFR galaxies, which is in agreement with the assessment of Fang et al. (2018). For lower-sSFR objects (i.e., transition and quiescent galaxies), $sSFR_{UV+IR}$ are systematically higher than $sSFR_{UV,cor}$. This inconsistency likely originates from the uncertainty of MIPS photometry (i.e., the deepest IR data available in GOODS-S and GOODS-N gives better consistency than the other three fields) or it is because the 24 μm flux in these objects comes, at least in part, from sources other than dust heated by conventional star formation (i.e., from old stars, see Fang et al. 2018, and references therein for discussions). For these reasons, it is reasonable to adopt the UV-based rates, especially when sSFR is low, as we do in this paper. In Figure 7, we replot the *UVJ* and *UVI* planes for the MIPS 24 μm detected subsample only, these time galaxies are color-coded by their log $sSFR_{UV+IR}$. Each individual is color-coded in the top two panels, whereas the median value in each bin is color-coded in the bottom two panels, which contains at least five objects. It can be seen that the main features, including the quenched region and the distinctive stripe patterns of sSFR, are statistically still strong when using independent UV+IR SFRs. This is in agreement with the result of Straatman et al. (2016, Figure 25), which strengthens our analysis in this work.

Appendix B
Sample Completeness

We discuss the resulting sample completeness by our selection criteria. First, the criterion $H_{\mathrm{mag}} < 24.5$ (criterion 1) can select relatively complete mass-limited samples of both blue and red galaxies above $M_* \sim 10^9\,M_\odot$ in the redshift range $z = 0.5$–1 (criterion 3; see Figure 2 in van der Wel et al. 2014). Second, `the SExtractor` parameter CLASS_STAR cut (criterion 2) is as powerful as colors are to separate galaxies from stars (see Figure 18 in Guo et al. 2013). Of particular note are the criteria 4–6. The `GALFIT` flag cut (criterion 4) excludes ≈4% of sample galaxies after the cuts 1–3. Visual inspection shows that these galaxies discarded by this cut are either mergers or strongly contaminated by neighbor objects. The multiaperture photometry on these objects by using the `IRAF` routine `ellipse` usually fails. Furthermore, to minimize the PSF effects on color measurement (see below), we applied the angular size cut, $R_{\mathrm{SMA}} > 3$ drizzled pixels (criterion 5). In Figure 8, we show the *UVJ* diagram, sSFR–mass relation and size–mass relation for both large and small galaxies after the cuts 1–4. As seen from the plots, the angular size cut preferentially removes more low-mass galaxies below $M_* \sim 10^{10.5}\,M_\odot$. This lack of sample completeness in this work cannot be avoided given the limited available resolution of *HST* images (Wang et al. 2017); otherwise, the resulting color gradients of very small galaxies are likely artificial. In Figure 9, we show that, in the sSFR–mass space, the

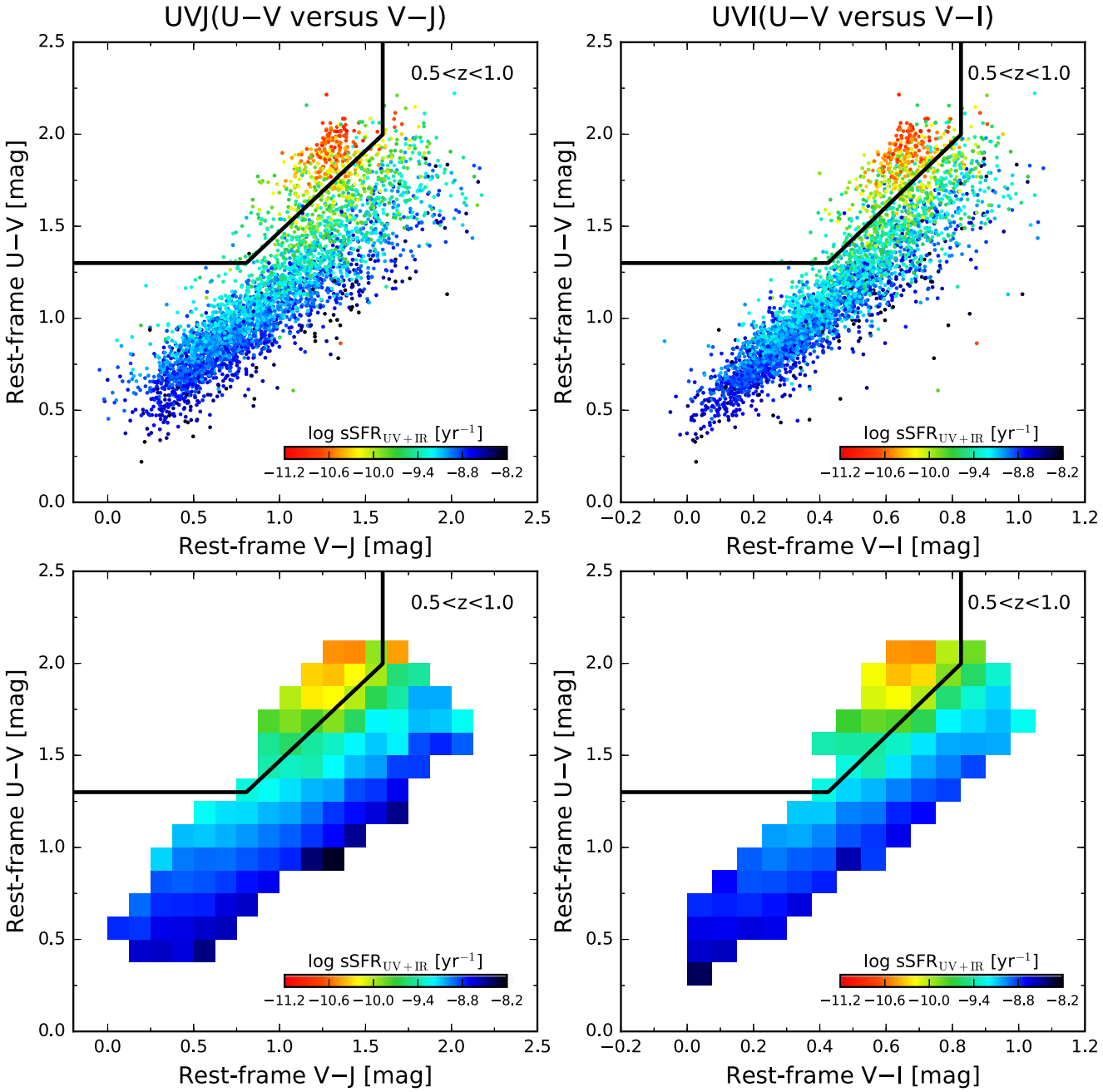

Figure 7. Rest-frame global *UVJ* diagrams (left) and *UVI* diagrams (right) for the MIPS 24 μm detected subsample after cuts 1–5, which are color-coded by log sSFR$_{UV+IR}$. Each individual is color-coded in the top two panels. In contrast, the median value in each bin is color-coded in the bottom two panels, which contains at least five objects. Solid lines have the same meanings as those in Figure 1.

distribution of galaxies satisfying criteria 1–6 is quite similar to that satisfying criteria 1–5, which indicates that criterion 6 does not create significant bias for this analysis. Finally, to enable the reader to know which bin is impacted the most, in Table 2, we specifically provide the resulting sample sizes by each cut after the third criterion for each subgroup in different mass bins.

Appendix C
PSF Effects on the Measurement of Color Gradients

In the documentation of the CANDELS *HST* multiband and multiaperture photometry catalogs still under construction by F. S. Liu et al. (2018, in preparation), we will make a detailed assessment of the PSF effects. So far, the effects of PSF mismatching and PSF smearing on derived color gradients have been evaluated as described below.

C.1. Effect of the PSF Mismatching

Stars should have no observed color gradients, so the color difference between any two observed bands should be zero at all radii. To check this, we have carefully selected some unsaturated stars brighter than 24 mag with CLASS_STAR $>$ 0.95 in the GOODS-S field. Figure 10 shows their integrated color differences between H(F160W) and bluer bands (J

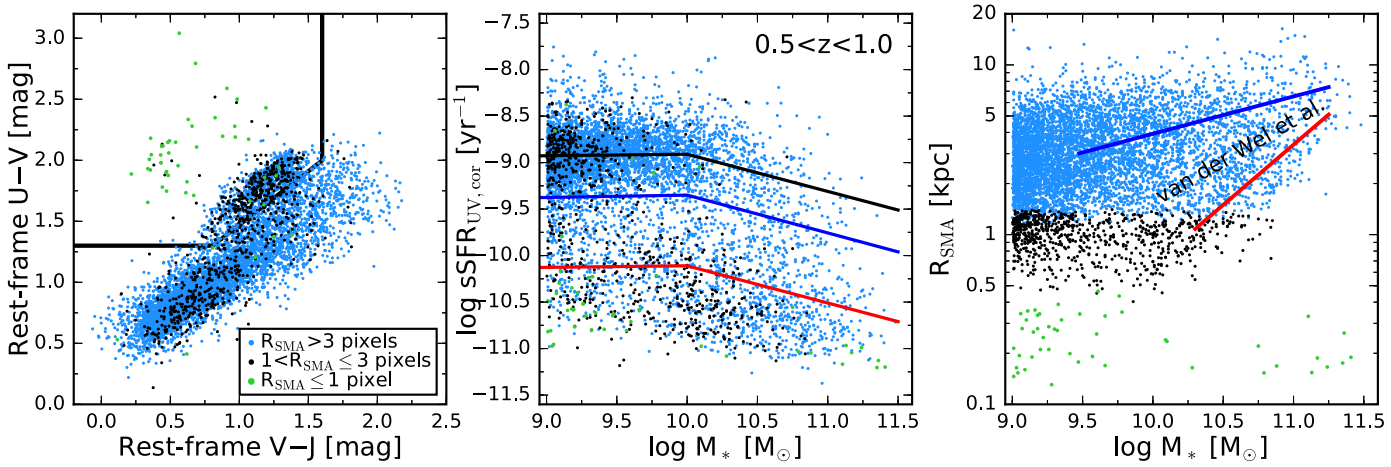

Figure 8. Rest-frame *UVJ* diagram (left), sSFR–mass relation (middle), and size–mass relation (right) for all galaxies after cuts 1–4. Galaxies are color-coded by their effective radii. Solid lines in the left panel have the same meanings as those in Figure 1. Solid lines in the middle panel have the same meanings as those in Figure 2. Solid lines in the right panel show the best-fit size–mass relations for star-forming galaxies with $M_* > 3 \times 10^9\ M_\odot$ (blue) and quiescent galaxies with $M_* > 2 \times 10^{10}\ M_\odot$ (red) determined by van der Wel et al. (2014), respectively. Note that no additional corrections on effective radii are applied here (see van der Wel et al. 2014, for details).

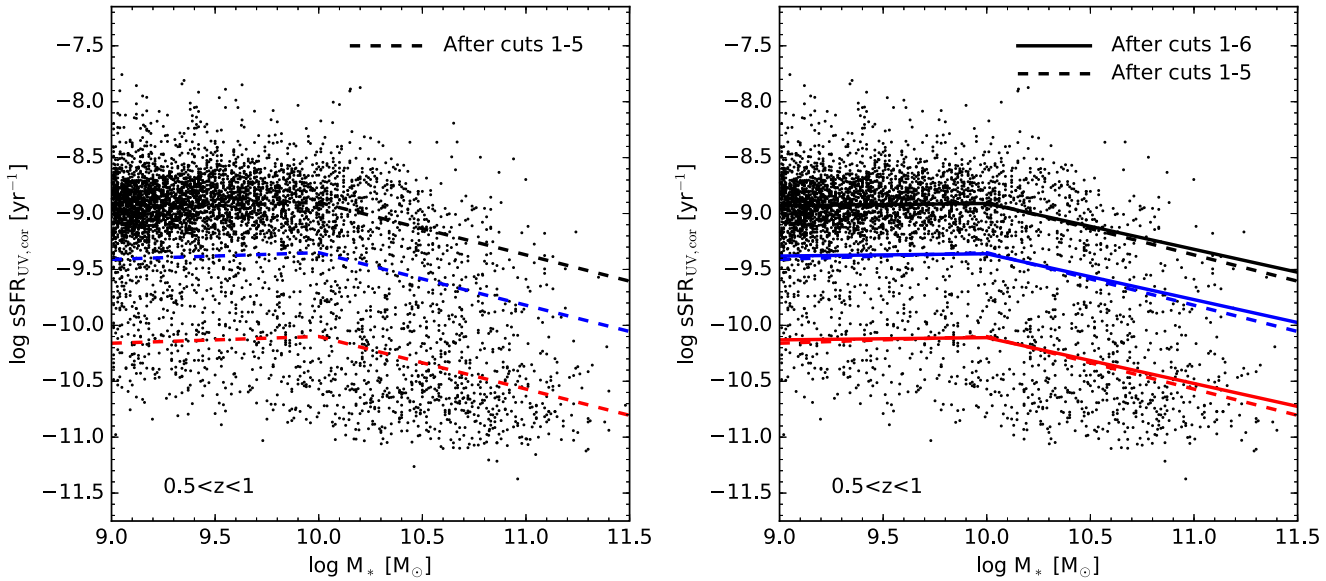

Figure 9. sSFR–mass relations for our sample of galaxies after cuts 1–5 (left) and that after cuts 1–6 (right). Black lines are the best broken power-law fits to the SFMS ($\Delta \log \mathrm{sSFR_{UV,cor}} = 0$). Blue lines indicate $\Delta \log \mathrm{sSFR_{UV,cor}} = -0.45$. Red lines indicate $\Delta \log \mathrm{sSFR_{UV,cor}} = -1.2$. As can be seen, the distribution of galaxies satisfying cuts 1–6 is quite similar to that satisfying cuts 1–5. The best-fit SFMS of galaxies after cuts 1–5 (dashed lines) can be described by the following equations: $\log \mathrm{sSFR_{UV,cor}}/\mathrm{yr}^{-1} = 0.06 \pm 0.03[\log M_*/M_\odot - 10] - 8.90 \pm 0.13$ for $M_* \leqslant 10^{10} M_\odot$, and $\log \mathrm{sSFR_{UV,cor}}/\mathrm{yr}^{-1} = -0.47 \pm 0.04[\log M_*/M_\odot - 10] - 8.90 \pm 0.13$ for $M_* > 10^{10}\ M_\odot$, which are only slightly different with the best-fit SFMS of our final sample (solid lines in the right panel; see Section 3).

(F125W), *I*(F814W), and *V*(F606W)). The result indicates that *V*(F606W) and *I*(F814W) are under-smoothed so the centers of the stars are bluer than the total colors (i.e., artificially bluer than what they should be). *J*(F125W) is over-smoothed so the centers are redder there. These trends are similar to those in the GOODS-S photometry paper (Guo et al. 2013). This is probably the best we can do with the IRAF/PSFMATCH program. At $R > 3$ pixels ($0\farcs18$), the median deviations (red circles) in *I*(F814W) and *J*(F125W) are almost zero. The deviation in *V*(F606W) is larger, but still less than ∼0.025 mag.

C.2. Effect of the PSF Smearing

Besides the mismatching issue among different bands addressed above, the effect of PSF smearing can also make the observed color gradients different from the intrinsic ones, especially for galaxies with small angular sizes and the galaxy central regions. We systematically evaluate this effect by modeling mock galaxies with various shapes and color gradients, and then convolve them with the F160W PSF to obtain smeared images, as we did for realistic galaxies. The color gradients of these output images are then compared with the intrinsic values. We assume that mock galaxies in one red

Table 2
The Resulting Sample Sizes by Each Cut after the Third Criterion for Each Subgroup in Different Mass Bins

Criteria	$9.0 < \log M_*/M_\odot \leqslant 9.5$	$9.5 < \log M_*/M_\odot \leqslant 10.0$	$10.0 < \log M_*/M_\odot \leqslant 10.5$	$\log M_*/M_\odot > 10.5$
		SFGs above the SFMS ridge (SFMS-upper)		
1–3	1524(100%)	662(100%)	282(100%)	64(100%)
1–4	1497(98.23%)	651(98.34%)	274(97.16%)	63(98.44%)
1–5	1319(86.55%)	629(95.02%)	269(95.39%)	62(96.88%)
1–6	1050(68.90%)	512(77.34%)	225(79.79%)	53(82.81%)
		SFGs below the SFMS ridge (SFMS-below)		
1–3	1174(100%)	486(100%)	210(100%)	85(100%)
1–4	1156(98.47%)	478(98.35%)	199(94.76%)	82(96.47%)
1–5	1036(88.25%)	459(94.44%)	194(92.38%)	82(96.47%)
1–6	842(71.72%)	374(76.95%)	148(70.48%)	65(76.47%)
		Transition galaxies		
1–3	344(100%)	220(100%)	212(100%)	196(100%)
1–4	326(94.77%)	217(98.64%)	199(93.87%)	188(95.92%)
1–5	258(75.00%)	168(76.36%)	174(82.08%)	185(94.39%)
1–6	185(53.78%)	131(59.55%)	134(63.21%)	153(78.06%)
		Quiescent galaxies		
1–3	240(100%)	230(100%)	345(100%)	322(100%)
1–4	204(85.00%)	201(87.39%)	325(94.20%)	296(91.93%)
1–5	117(48.75%)	117(50.87%)	212(61.45%)	264(81.99%)
1–6	82(34.17%)	82(35.65%)	147(42.61%)	194(60.25%)

band have ideal single-component Sérsic profiles, with $R_{\rm SMA} = 0.2, 0.35, 0.5, 0.65$ arcsec (note that the drizzled imaging pixel scale is 0.06 arcsec/pixel), Sérsic index $n = 0.5, 1.0, 1.5, 2.0$ and ellipticity $\epsilon = 0.0, 0.3, 0.5, 0.7$ well represent the majority of realistic galaxies. Then one of logarithmic color gradients $G = d\text{color}/d\ \log\ r = -0.1, -0.3, -0.5$ is superimposed onto the Sérsic profile, except that a linear component is adopted for the central pixel instead to avoid logarithmic divergence, as the image of the other bluer band. The observed normalized color gradients are then compared to the unsmeared unit color gradient.

In Figure 11, we show the results for these mock galaxies with typical shapes and gradients (median values). Zero points are all fixed at $R_{\rm SMA}$. It can be seen that the deviation is quickly enlarged after the radial distance decreases to 3 pixel sizes ($0\farcs18$), suggesting that PSF smearing effect roughly diminishes at 0.18 arcsec away from galaxy centers. Therefore, it is reasonable to exclude small galaxies with effective radii less than $0\farcs18$ and take the color of $R > 0\farcs18$ as a safe indicator of the intrinsic color. In conclusion, the overall PSF effects are not large for real data at $R > 0\farcs18$. The PSF correction can result in an error of $\sim$0.05 in our color gradients at most (also see Figure 5 in Wang et al. 2017).

Appendix D
Error Estimate on the Stacked Color Trajectories

In Figures 3 and 4, we provide the typical errors of the stacked colors in each panel, which are the average of the standard errors of median colors at all radii. Figure 12 presents an example to illustrate our estimate on the standard errors of the median colors at a given radius. For the *UVI* colors at $R_{\rm SMA}$ of face-on SFMS-upper galaxies in the mass bin $M_* = 10^{10}$–$10^{10.5}\ M_\odot$, the photometric errors (i.e., read-out noise, sky subtraction, and PSF matching, etc.) of individual data points are typically 0.1–0.15 mag (left). The standard error of the median $U - V$ or $V - I$ colors at this radius is computed using a Monte Carlo simulation to regenerate 1000 realizations of median colors after resampling at each iteration of the errors of each data point from Gaussian distribution, with zero means and standard deviations given by the observed photometric errors. The resulting 1000 median colors are assumed to follow a Gaussian distribution. The standard error of the median colors at this radius is roughly the same as the standard deviation of the assumed Gaussian distribution (right).

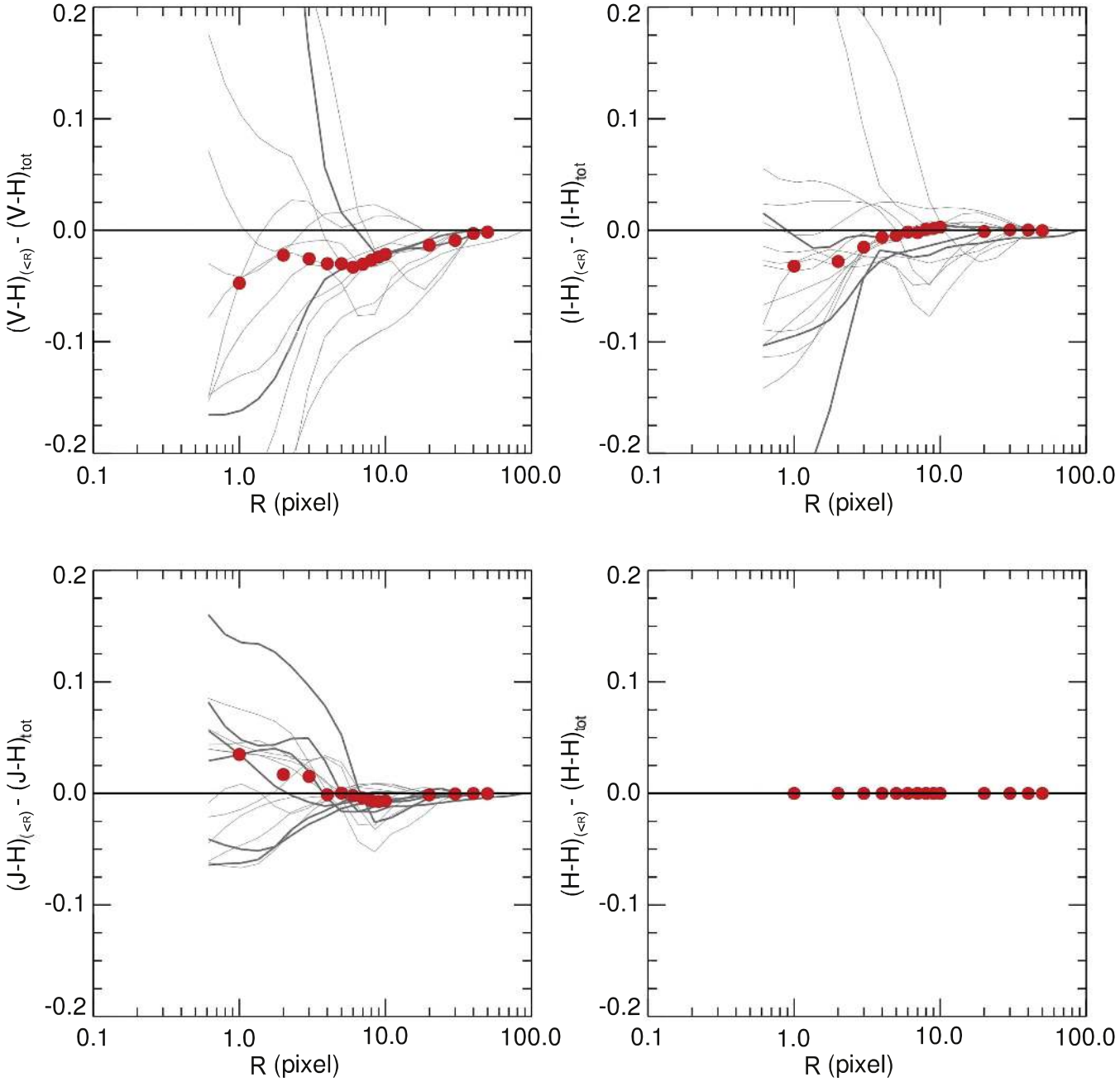

Figure 10. Integrated color differences between H(F160W) and bluer bands (J(F125W), I(F814W), and V(F606W)) for unsaturated stars brighter than 24 mag in the H (F160W) band in the GOODS-S field. Gray lines show individual stars. Red circles show the medians. Stars should have no observed color gradients, so the difference between any two bands should be zero at all radii. This check shows that V and I are under-smoothed so the centers of the stars are bluer than the total colors (i.e., artificially bluer than what they should be). J is over-smoothed so the centers are redder there. At $R > 3$ pixels, the deviations of the red circles in I and J are almost zero. The deviation in V is larger, but still less than $\sim$0.025 mag.

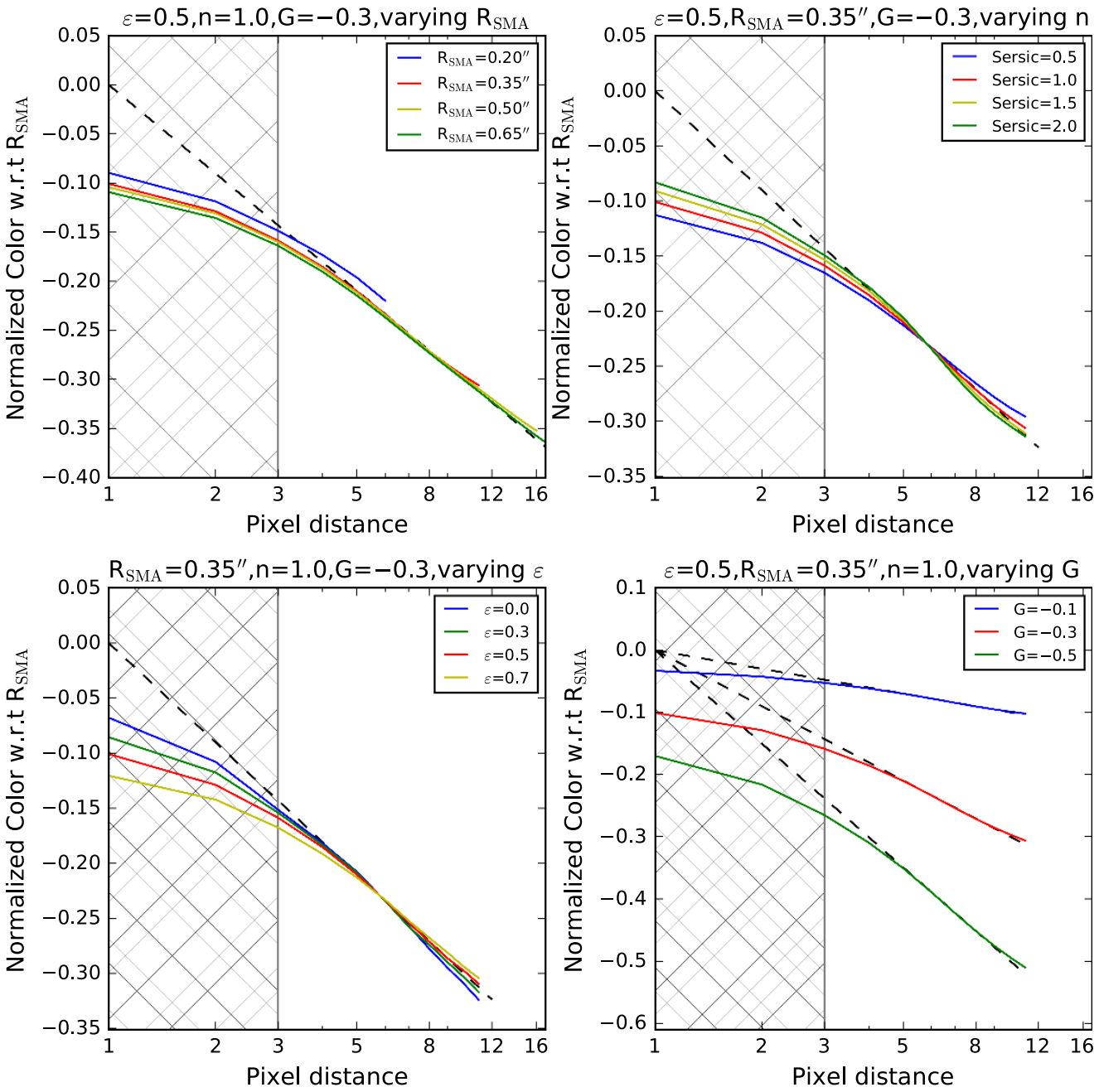

Figure 11. Normalized smeared color gradients in comparison with the intrinsic unit logarithmic gradients (G) for mock galaxies with different $R_{\rm SMA}$, ellipticity (ϵ), and Sérsic index. Zero points are all fixed at $R_{\rm SMA}$.

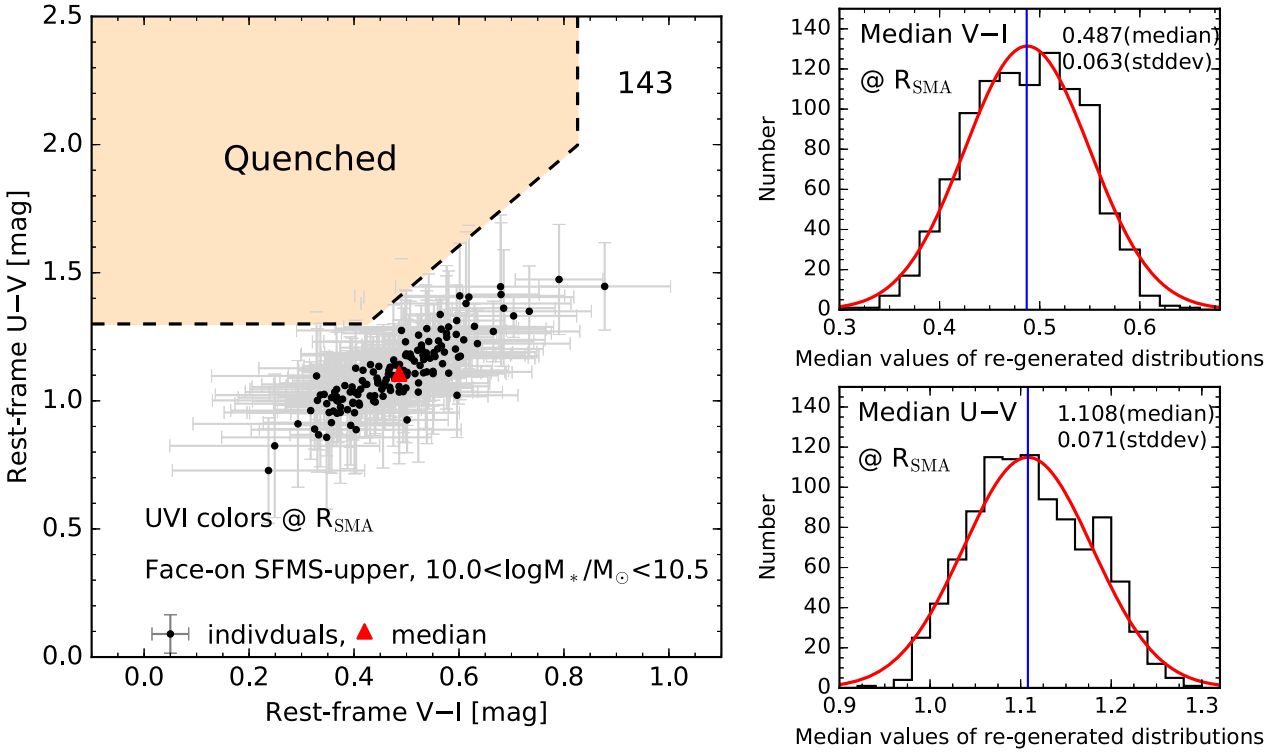

Figure 12. Example to illustrate our estimate on the standard errors of median colors at a given radius in a given panel. Left panel shows the UVI color distribution at R_{SMA} for face-on SFMS-upper galaxies in the mass bin $M_* = 10^{10}$–$10^{10.5}$ $M_\odot$. The observed photometric errors (i.e., readout noise, sky subtraction, and PSF matching, etc.) of individual points are given, which are typically 0.1–0.15 mag. Median values are shown with a red triangle. The standard error of the median $U - V$ or $V - I$ colors at this radius is computed using a Monte Carlo simulation to regenerate 1000 realizations of median colors after resampling at each iteration of the errors of each data point from Gaussian distribution, with zero means and standard deviations given by the observed photometric errors. Right panels show the distributions of these newly generated median $U - V$ and $V - I$ colors. The standard deviations are computed by assuming their distributions follow a Gaussian form. The galaxy number in this panel is shown on the right-top corner.

ORCID iDs

F. S. Liu https://orcid.org/0000-0002-1064-1544
Hassen M. Yesuf https://orcid.org/0000-0002-4176-9145
David C. Koo https://orcid.org/0000-0003-3385-6799
Yicheng Guo https://orcid.org/0000-0003-2775-2002
Eric F. Bell https://orcid.org/0000-0002-5564-9873
Dongfei Jiang https://orcid.org/0000-0003-0414-1479
Anton M. Koekemoer https://orcid.org/0000-0002-6610-2048
Xianzhong Zheng https://orcid.org/0000-0003-3728-9912
Guillermo Barro https://orcid.org/0000-0001-6813-875X
Pablo G. Pérez-González https://orcid.org/0000-0003-4528-5639
Avishai Dekel https://orcid.org/0000-0003-4174-0374
Nimish P. Hathi https://orcid.org/0000-0001-6145-5090
Darren Croton https://orcid.org/0000-0002-5009-512X

References

Barro, G., Faber, S. M., Koo, D. C., et al. 2017, ApJ, 840, 47
Belfiore, F., Maiolino, R., Bundy, K., et al. 2017, arXiv:1710.05034
Brammer, G. B., van Dokkum, P. G., & Coppi, P. 2008, ApJ, 686, 1503
Brammer, G. B., Whitaker, K. E., van Dokkum, P. G., et al. 2011, ApJ, 739, 24
Brinchmann, J., Charlot, S., White, S. D. M., et al. 2004, MNRAS, 351, 1151
Bruzual, G., & Charlot, S. 2003, MNRAS, 344, 1000
Calzetti, D., Armus, L., Bohlin, R. C., et al. 2000, ApJ, 533, 682
Chabrier, G. 2003, PASP, 115, 763
Croton, D. J., Springel, V., White, S. D. M., et al. 2006, MNRAS, 365, 11
Dahlen, T., Mobasher, B., Faber, S. M., et al. 2013, ApJ, 775, 93
Elbaz, D., Daddi, E., Le Borgne, D., et al. 2007, A&A, 468, 33
Fang, J. J., Faber, S. M., Koo, D. C., et al. 2018, ApJ, 858, 100
Fang, J. J., Faber, S. M., Koo, D. C., & Dekel, A. 2013, ApJ, 776, 63
Galametz, A., Grazian, A., Fontana, A., et al. 2013, ApJS, 206, 10
Geach, J. E., Hickox, R. C., Diamond-Stanic, A. M., et al. 2014, Natur, 516, 68
Geha, M., Blanton, M. R., Yan, R., & Tinker, J. L. 2012, ApJ, 757, 85
Grogin, N. A., Kocevski, D. D., Faber, S. M., et al. 2011, ApJS, 197, 35
Guo, Y., Bell, E. F., Lu, Y., et al. 2017, ApJL, 841, L22
Guo, Y., Ferguson, H. C., Giavalisco, M., et al. 2013, ApJS, 207, 24
Jedrzejewski, R. I. 1987, MNRAS, 226, 747
Jiang, D., Liu, F. S., Zheng, X., et al. 2018, ApJ, 854, 70
Kawinwanichakij, L., Papovich, C., Quadri, R. F., et al. 2017, ApJ, 847, 134
Kennicutt, R. C., & Evans, N. J. 2012, ARA&A, 50, 531
Koekemoer, A. M., Faber, S. M., Ferguson, H. C., et al. 2011, ApJS, 197, 36
Kriek, M., van Dokkum, P. G., Labbé, I., et al. 2009, ApJ, 700, 221
Laidler, V. G., Papovich, C., Grogin, N. A., et al. 2007, PASP, 119, 1325
Lee, N., Sanders, D. B., Casey, C. M., et al. 2015, ApJ, 801, 80
Liu, F. S., Jiang, D., Faber, S. M., et al. 2017, ApJL, 844, L2
Liu, F. S., Jiang, D., Guo, Y., et al. 2016, ApJL, 822, L25
Momcheva, I. G., Brammer, G. B., van Dokkum, P. G., et al. 2016, ApJS, 225, 27
Morris, A. M., Kocevski, D. D., Trump, J. R., et al. 2015, AJ, 149, 178
Nayyeri, H., Hemmati, S., Mobasher, B., et al. 2017, ApJS, 228, 7
Nelson, E. J., Tadaki, K.-i., Tacconi, L. J., et al. 2018, arXiv:1801.02647
Nelson, E. J., van Dokkum, P. G., Brammer, G., et al. 2012, ApJL, 747, L28
Nelson, E. J., van Dokkum, P. G., Förster Schreiber, N. M., et al. 2016a, ApJ, 828, 27
Nelson, E. J., van Dokkum, P. G., Momcheva, I. G., et al. 2016b, ApJL, 817, L9
Noeske, K. G., Weiner, B. J., Faber, S. M., et al. 2007, ApJL, 660, L43
Papovich, C., Kawinwanichakij, L., Quadri, R. F., et al. 2018, ApJ, 854, 30
Pan, Z., Li, J., Lin, W., et al. 2015, ApJL, 804, L42
Patel, S. G., Kelson, D. D., Holden, B. P., Franx, M., & Illingworth, G. D. 2011, ApJ, 735, 53
Peng, C. Y., Ho, L. C., Impey, C. D., & Rix, H.-W. 2002, AJ, 124, 266
Peng, Y.-j., Lilly, S. J., Kovač, K., et al. 2010, ApJ, 721, 193

Peng, Y.-j., Lilly, S. J., Renzini, A., & Carollo, M. 2012, ApJ, 757, 4
Pérez, E., Cid Fernandes, R., González Delgado, R. M., et al. 2013, ApJL, 764, L1
Rujopakarn, W., Rieke, G. H., Weiner, B. J., et al. 2013, ApJ, 767, 73
Santini, P., Ferguson, H. C., Fontana, A., et al. 2015, ApJ, 801, 97
Sérsic, J. L. 1968, Atlas de Galaxias Australes (Cordoba: Observatorio Astronomico)
Stefanon, M., Yan, H., Mobasher, B., et al. 2017, ApJS, 229, 32
Straatman, C. M. S., Spitler, L. R., Quadri, R. F., et al. 2016, ApJ, 830, 51
Szomoru, D., Franx, M., Bouwens, R. J., et al. 2011, ApJL, 735, L22
Tacchella, S., Carollo, C. M., Forster Schreiber, N. M., et al. 2018, ApJ, 859, 56
Tacchella, S., Dekel, A., Carollo, C. M., et al. 2016a, MNRAS, 458, 242
Tacchella, S., Dekel, A., Carollo, C. M., et al. 2016b, MNRAS, 457, 2790
Tomczak, A. R., Quadri, R. F., Tran, K.-V. H., et al. 2016, ApJ, 817, 118
van der Wel, A., Bell, E. F., Häussler, B., et al. 2012, ApJS, 203, 24
van der Wel, A., Franx, M., van Dokkum, P. G., et al. 2014, ApJ, 788, 28
Wang, W., Faber, S. M., Liu, F. S., et al. 2017, MNRAS, 469, 4063
Whitaker, K. E., Bezanson, R., van Dokkum, P. G., et al. 2017, ApJ, 838, 19
Whitaker, K. E., Franx, M., Leja, J., et al. 2014, ApJ, 795, 104
Williams, R. J., Quadri, R. F., Franx, M., van Dokkum, P., & Labbé, I. 2009, ApJ, 691, 1879
Wu, H., Shao, Z., Mo, H. J., Xia, X., & Deng, Z. 2005, ApJ, 622, 244
Wuyts, S., Förster Schreiber, N. M., Genzel, R., et al. 2012, ApJ, 753, 114
Wuyts, S., Förster Schreiber, N. M., Lutz, D., et al. 2011, ApJ, 738, 106
Wuyts, S., Förster Schreiber, N. M., Nelson, E. J., et al. 2013, ApJ, 779, 135
Wuyts, S., Labbé, I., Franx, M., et al. 2007, ApJ, 655, 51